ADVANCED MATERIALS INTERFACES
www.advmatinterfaces.de

Uncapped Gold Nanoparticles for the Metallization of Organic Monolayers

Alba Martín-Barreiro, Rogelio Soto, Stefano Chiodini, Aitor García-Serrano, Santiago Martín, Lucía Herrer, Francesc Pérez-Murano, Paul J. Low, José Luis Serrano, Susana de Marcos, Javier Galban, and Pilar Cea**

Deposition of the top-contact electrode to create large-area electrode | monolayer | electrode junctions represents a contemporary challenge to the integration of molecular electronic phenomena into device structures. Here, a top contact electrode is formed on top of an organic monolayer over a large area (cm^2) by two simple, sequential self-assembly steps. Initial self-assembly of 4,4′-(1,4-phenylenebis(ethyne-2,1-diyl))dianiline onto gold-on-glass substrates gives high-quality monolayers. The exposed amine functionality is subsequently used to anchor uncapped gold nanoparticles deposited in a second self-assembly step. These uncapped gold nanoparticles are prepared by thermolysis of lipoic acid stabilized gold nanoclusters and contain gold oxide (≈9%) that provides stability in the absence of an organic capping ligand. This two-step procedure results in full coverage of the monolayer by the densely packed gold nanoparticles, which spontaneously condense to give a semi-continuous film. The electrical properties of these junctions are determined from *I–V* curves, revealing uniform electrical response and absence of metallic short-circuits or evidence of damage to the underlying molecular monolayer. These promising electrical characteristics suggest that the deposition of uncapped gold nanoparticles on suitably functionalized molecular monolayers provides a path for the fabrication of molecular electronic devices using simple methodologies.

1. Introduction

The field of molecular electronics is concerned with the use of molecular properties to permit, control, and manipulate electrical transmission between two electrodes.[1,2] The fundamental tool for exploration is the electrode | molecule | electrode 'molecular junction'.[3–6] The design of the molecular junction aligns with much of the early motivation for the pursuit of molecular electronics, which has been based on the concept that an appropriately designed molecule would be capable as performing one (or more) of the basic functions of a circuit element. To this end, molecules that perform the functions of wires,[7] switches,[8] diodes,[9] rectifiers,[10] transistors,[11] and highly efficient resistors[12] have been designed and their electrical characteristics within a junction demonstrated.

More recently attention has turned to properties of molecular junctions that extend beyond the mimicry of electrical

A. Martín-Barreiro, S. de Marcos, J. Galban
Departamento de Química Analítica
Facultad de Ciencias
Universidad de Zaragoza
Zaragoza 50009, Spain
E-mail: jgalban@unizar.es

A. Martín-Barreiro, R. Soto, S. Chiodini, A. García-Serrano, S. Martín, L. Herrer, J. L. Serrano, S. de Marcos, J. Galban, P. Cea
Instituto de Nanociencia y Materiales de Aragón (INMA)
Universidad de Zaragoza-CSIC
Zaragoza 50009, Spain
E-mail: pilarcea@unizar.es

S. Chiodini, A. García-Serrano, S. Martín, L. Herrer, P. Cea
Departamento de Química Física
Facultad de Ciencias
Universidad de Zaragoza
Zaragoza 50009, Spain

The ORCID identification number(s) for the author(s) of this article can be found under https://doi.org/10.1002/admi.202100876.

© 2021 The Authors. Advanced Materials Interfaces published by Wiley-VCH GmbH. This is an open access article under the terms of the Creative Commons Attribution-NonCommercial-NoDerivs License, which permits use and distribution in any medium, provided the original work is properly cited, the use is non-commercial and no modifications or adaptations are made.

DOI: 10.1002/admi.202100876

S. Chiodini, S. Martín, L. Herrer, P. Cea
Laboratorio de Microscopias Avanzadas (LMA) Campus Río Ebro
Universidad de Zaragoza
C/Mariano Esquilor, s/n, Zaragoza 50018, Spain

F. Pérez-Murano
Instituto de Microelectrónica de Barcelona (IMB-CNM CSIC)
Campus UAB
Bellaterra 08193, Spain

P. J. Low
School of Molecular Sciences
University of Western Australia
35 Stirling Highway, Crawley, Perth 6009, Australia

J. L. Serrano
Departamento de Química Orgánica
Facultad de Ciencias
Universidad de Zaragoza
Zaragoza 50009, Spain

components at the single-molecule level. Various studies have now shown that molecular junctions may have applications in areas as diverse as solar-energy harvesting,[13] thermoelectric conversion,[14,15] and molecular sensing,[16,17] whilst single-molecule light-emitting diodes have also been demonstrated.[18] Mechanical manipulation of molecules within the junction has led to interests in mechanically switched molecular electronic components,[19,20] whilst single-molecule reactions within the junction have emerged as a hot topic area in recent years.[21,22]

As a consequence of the many phenomena exhibited within molecular junctions and the potential applications that may arise, both single-molecule and 'large-area' junctions attract attention. The analysis of the fundamental properties of single-molecule junctions has proven essential to developing an understanding of the key parameters that determine the electrical properties of molecular junctions (e.g., the chemical structure of the molecular backbone, the composition and position of molecule-electrode anchoring groups, molecular conformation, the role of metal complexation, sensitivity of the junction to molecular redox state, the nature of the electrode material, solvation, etc.).[23] The ability to precisely control the molecular length and chemical composition of single molecules and to carry out high-level computational studies on single-molecule junctions has allowed detailed investigations of the various mechanisms that mediate electronic transport in molecular junctions, giving great insight into future molecular design principles.[24–26]

Whilst single-molecule junctions have proven to be immensely powerful research tools, 'large-area' molecular electronic devices, where millions of molecules are arranged in a parallel fashion and assembled between the terminal electrodes, arouse interest due to the potential of such structures to incorporate molecular electronic effects into real devices.[27,28] The development of large-area molecular junctions is due in no small part to the maturity of the processes for deposition of high-quality monolayer films onto (semi)conducting substrates by vacuum deposition, Langmuir–Blodgett techniques, self-assembly methods, and electrografting processes. These films can be contacted directly by a conducting AFM, STM tip or within a cross-wire device[29] to form the junction, or further functionalized by deposition of a metallic nanoparticle to create a nascent electrode | monolayer | nanoparticle multi-molecule junctions. However, one of the main bottlenecks to be addressed en route to true large-area molecular electronic junctions is the development of methodologies that permit top electrodes to be reliably fabricated onto the functional monolayer.[30–36]

A variety of different approaches toward the deposition of a top contact electrode onto a monolayer have been explored, including: evaporation techniques (direct and indirect evaporation as well as insertion of a buffer interlayer between the top contact and the organic film);[5,37–45] liquid metals;[5,41,46,47] eC electron beam deposition,[48] and focused electron beam induced deposition;[49] flip-chip lamination;[41,50] nanotransfer imprinting lithography;[51] electrodeposition;[52–54] surface-diffusion-mediated deposition;[54] photoreduction of metal precursors;[55,56] chemisorption of freshly prepared uncapped metal nanoparticles onto terminal functionalized monolayers;[57,58] and the thermal induced decomposition of an organometallic compound.[59,60] However, whilst each of these methods has a particular advantage and have met with a degree of success, various problems are often encountered when a thin layer of a conducting material is deposited onto a monolayer of a soft material which makes translation of the junctions from laboratory to a production scale difficult. These problems include penetration of high-energy metal atoms through the monolayer during the deposition process resulting in short-circuits and/or damage of the functional organic molecules in the monolayer, and low surface coverage of the monolayer by the top-contact electrode.[30–36] Whilst the use of liquid materials as top contacts alleviates some of these issues, a liquid contact would force the use of encapsulation techniques that may not be compatible with large-scale fabrication whilst also being reliant on toxic (Hg) or scarce (e-GaIn) materials. The use of electron-beam deposited carbon electrodes has met with great success in the fabrication of molecular junctions from robust molecular layers, but the nature of the equipment involved means that this technique is not readily accessible in many laboratories. Recently, Puebla-Hellmann et al.[61] have deposited gold nanoparticles stabilized by weakly bound ligands onto SAMs of alkanedithiols. These SAMs were constrained in circular pores of variable diameter, from 70 μm to 60 nm. The subsequent deposition of a thin gold film by PVD (physical vapor deposition) served to create an electrical contact among the particles. This methodology resulted in high yield and high device-to-device reproducibility, providing a new route to large-scale integration of molecular compounds.

In terms of the composition of the top-contact electrode, whilst not without issues or competition, gold remains the most commonly used electrode material in molecular electronics. The use of gold as the bottom-electrode in the field of molecular electronics has been persistent due to the confluence of several properties including its noble character, facile fabrication into high-quality films with large-area atomically flat terraces, high conductivity, and good environmental stability. Critically, gold also has the ability to support the formation of excellent quality monolayers with the relatively strong gold-molecule contacts through, for example, thiol, amine, carboxylate, pyridine, and functional groups. In addition to its role as a substrate electrode, gold has also attracted much attention as a top-contact electrode material in forms from gold nanoclusters (AuNC) and nanoparticles (AuNPs) to continuous metal thin films. Whilst continuous metal films are in demand for the integration of molecular electronics into device structures, gold-based nanomaterials exhibit interesting redox properties (which make them suitable for hybrid electronic devices[62]), low toxicity, and excellent biocompatibility, which attracts interest in a future biocompatible electronics,[63,64] and spectroscopic properties, which are reflected in their wide applications for imaging and sensing.[65] This last property is highly dependent on the particle size.[66] Thus, AuNPs have a continuous density of energy states that results in a surface plasmon, the maximum absorption wavelength of which depends on the diameter of the particle.[67] This property makes AuNP very interesting for colorimetric sensors[68–70] and SERS substrates.[71,72] In contrast, AuNC are not able to support surface plasmons, but present molecular-like energy transitions that provide them with fluorescent properties making them suitable for use as fluorescent sensors.[73,74]

All these properties depend to a large extent on the external shell surrounding the nanomaterial and the stabilizing

© 2021 The Authors. Advanced Materials Interfaces published by Wiley-VCH GmbH

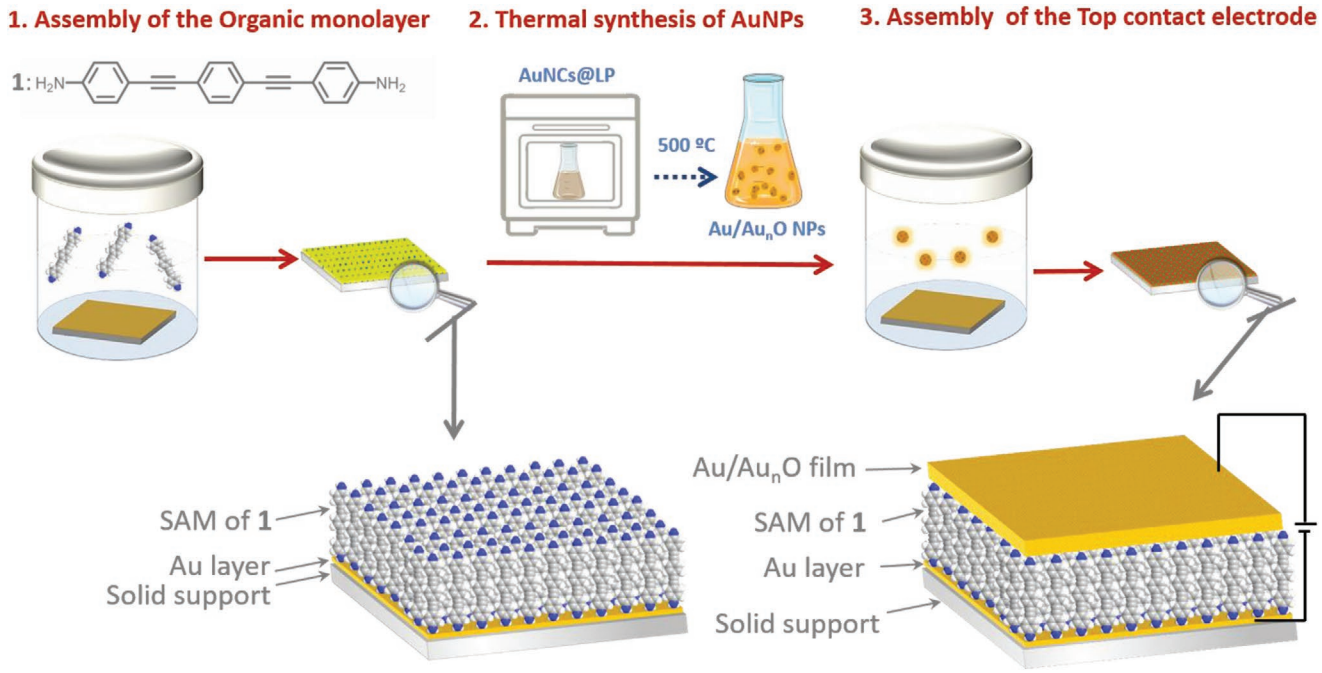

Figure 1. Cartoon showing the fabrication process followed in this contribution for the preparation of Au | SAM of **1** | (Au/Au$_n$O)NP molecular junctions. As described in the text, the organic monolayer is first self-assembled onto the bottom electrode (1). Gold nanoparticles are syntetized by thermolysis of precursor lipoic acid stabilized gold nanoclusters (2). The generated gold nanoparticles are subsequently deposited onto the organic monolayer to form the top-contact electrode (3).

surfactants used to prevent aggregation may modify or hinder many applications of AuNPs as top-contact electrode materials. Conversely, naked gold nanomaterials, that is, nanomaterials without capping agents and presenting metal or metal oxide surfaces, present better electric and spectroscopic properties than analogous particles capped with ligands,[75,76] but have greater tendencies toward aggregation, which has limited their applications as true nanomaterials. Laser ablation (LAL) of a gold target in liquid phase[77] has been adopted as an alternative method to synthesize stable AuNPs without the need of surfactant-like capping ligands to prevent aggregation. The LAL-generated AuNPs are negatively charged because of their partial oxidization to Au^{1+} or even Au^{2+} and Au^{3+} and subsequent adsorption of hydroxyl anions from the aqueous media, which contribute to the electrostatic stabilization of the synthetized AuNPs and prevent aggregation.[78] Analyses of LAL-generated nanoparticles by X-ray photoelectron spectroscopy (XPS) indicate that a variable percentage of the surface gold atoms are oxidized, typically around a 10%,[79] albeit that the precise value is dependent on the surrounding electrolyte[78] as well as on the size of the nanoparticles and the underlying substrate where these particles are deposited for the spectroscopic studies.[78]

Motivated by the above mentioned advances in the fabrication of the top-contact electrode in molecular electronics, as well as the success in the use of gold nanoparticles as a physical shield that dissipates the kinetic energy of the metal atoms in the subsequent PVD process, here, we extend these ideas to the further search of wet self-assembled technologies for the top-contact deposition. These contributions greatly simplify the preparation of top-contacts for molecular junctions based on simple physicochemical processes, which is readily scalable, and uses fewer reagents and fabrication steps and less energy than current technologies. In particular, in this contribution we consider the use of surfactant-free gold nanoparticles synthesized by thermolysis of lipoic acid stabilized AuNC. The gold nanoparticles prepared in this manner are stabilized in an aqueous media due to the presence of oxidized gold atoms (≈9% of gold is Au$_n$O) and possibly adsorption of hydroxyl anions in the same manner as the LAL-generated AuNPs. These gold nanoparticles, hence forward named as (Au/Au$_n$O)NPs, have been self-assembled onto a monolayer film of the α,ω-bis(amine)-functionalized 'wire-like' molecule 4,4′-(1,4-phenylenebis(ethyne-2,1-diyl))dianiline (**1**) (**Figure 1**). The resulting Au | SAM of **1** | (Au/Au$_n$O)NPs junctions exhibit a large surface coverage of the monolayer by the (Au/Au$_n$O) NPs, which condense to give a semi-continuous thin film with high yields (i.e., the electrical measurements do not show evidence of short-circuits). This fabrication methodology is presented here as a proof-of-concept study that holds considerable promise for use in the metallization of organic monolayers and future creation of large-area molecular electronic junctions.

2. Results and Discussion

Uncapped gold nanoparticles were prepared by thermolysis of lipoic acid stabilized AuNC (AuNCs@LP).[80] Thermolysis temperatures from 300 to 700 °C were explored (Supporting Information), the gold nanoparticles prepared by thermolysis at 500 °C being selected for this study (Figure 1). The UV–vis spectrum of an aqueous dispersion of the gold nanoparticles synthesized at 500 °C featured maxima at 530 and 690 nm consistent with two populations (Figure S1A, Supporting Information);

© 2021 The Authors. Advanced Materials Interfaces published by Wiley-VCH GmbH

the population responsible for the longer wavelength absorbance being attributed to aggregation of the smaller particles responsible for the 530 nm population (Figure S1A, Supporting Information). In addition, the fluorescence contour plot of these gold nanoparticles shows a large emission maximum at 400 nm upon excitation at 320 nm (Figure S1B, Supporting Information). These optical properties are consistent with quantized metal gold nanoparticles. Further examination of the gold nanoparticles dispersed on Cu^0 grids by scanning transmission electron microscopy (STEM; Figure S2A, Supporting Information) also indicates the presence of two gold nanoparticles populations formed at 500 °C, one with diameter of 3.95 ± 1.08 nm and a more abundant population with diameter 13.66 ± 3.37 nm (Figure S2B, Supporting Information). These gold nanoparticles were also characterized by dynamic light scattering (DLS, Figure S2C, Supporting Information) showing a main hydrodynamic radius of 12.5 nm coincident with the most abundant population observed by STEM and two other less abundant populations around 15.5 and 19.5 nm attributed to the minority nanoparticles that have grown with temperature and present the absorption around 690 nm. The zeta potential of the nanoparticles was determined to be −43.82 ± 0.63 mV thus giving evidence that the particles were capped by negative ions leading to a negative zeta potential.

In contrast to the XPS spectrum of the precursor AuNCs@LP, which exhibits the expected $4f_{7/2}$ and $4f_{5/2}$ peaks for Au(0) at 84.0 and 87.8 eV, the XPS of the gold nanoparticles reveals a shift of the gold peaks toward lower binding energies as the pyrolysis temperature increases (Figure S3, Supporting Information). The XPS spectrum of the particles formed at 500 °C features peaks at 83.3 ($4f_{7/2}$) and 87.0 eV ($4f_{5/2}$). The shift of the Au(0) peaks to lower binding energies has been attributed to two effects.[81] On the one hand, the increase in the size of gold nanoparticles that occurs upon the pyrolysis implies a charge redistribution that leads to lower binding energies. On the other hand, the initial AuNC stabilized with lipoic acid feature a strong covalent bond (S—Au) that involves a transfer of charge from gold to sulphur. As the temperature increases and this organic capping agent is eliminated, the surface energy of gold atoms is reduced through the rehybridization of the Au atoms on the surface and the particle core with an increase in the d–d interaction. In addition to the Au(0) peaks, the XPS spectrum at 500 and 700 °C also exhibits two peaks at 84.7 and 88.3 eV, attributable to gold oxides. Whilst the presence of Au_2O_3 shifts the metal peaks by 1.8 eV or more,[82,83] lower oxide species such as AuO and Au_2O exhibit peaks shifted by 1.5 eV or even less in comparison with the metal.[84] Therefore, the peaks at 84.7 and 88.3 eV are tentatively assigned here to lower gold oxides. A quantitative study of the peak areas indicates that the ratio of gold oxide for the gold nanoparticles prepared from thermolysis of AuNCs@LP at 500 °C is ≈9% (Figure S3, Supporting Information). For this reason, the gold nanoparticles used in this contribution which were prepared by thermolysis at 500 °C are denoted (Au/Au_nO)NPs. An XPS survey spectrum over a wide range of binding energies (Figure S4, Supporting Information) shows that the pristine (Au/Au_nO)NPs do not show significant evidences of extraneous materials that could be adsorbed from air (typically thiols, amines, chlorides, etc.). In addition, to avoid any potential contamination from air, the (Au/Au_nO)NPs were dispersed in Milli-Q water, and the metallization process of the monolayers was performed with such a dispersion.

Self-assembled monolayers (SAMs) of compound **1** were prepared on flame-annealed gold-on-mica substrates (Figure 1).[58] These SAMs of **1** have been characterized previously,[58] and additional information about their preparation and characterization is also reported in the Experimental Section and in the Supporting Information of this contribution. In brief, the surface coverage of the SAM of **1** onto a gold substrate was 8.02×10^{-10} mol·cm^{-2} (equivalent to an area per molecule of 0.20 nm^2·molecule) as determined using a quartz crystal microbalance (QCM). This surface density is indicative of the formation of tightly-packed SAM monolayers. The formation of a tightly packed monolayer was further probed by cyclic voltammetry (CV) using a $K_3[Fe(CN)_6]$ redox probe.[85,86] The SAM

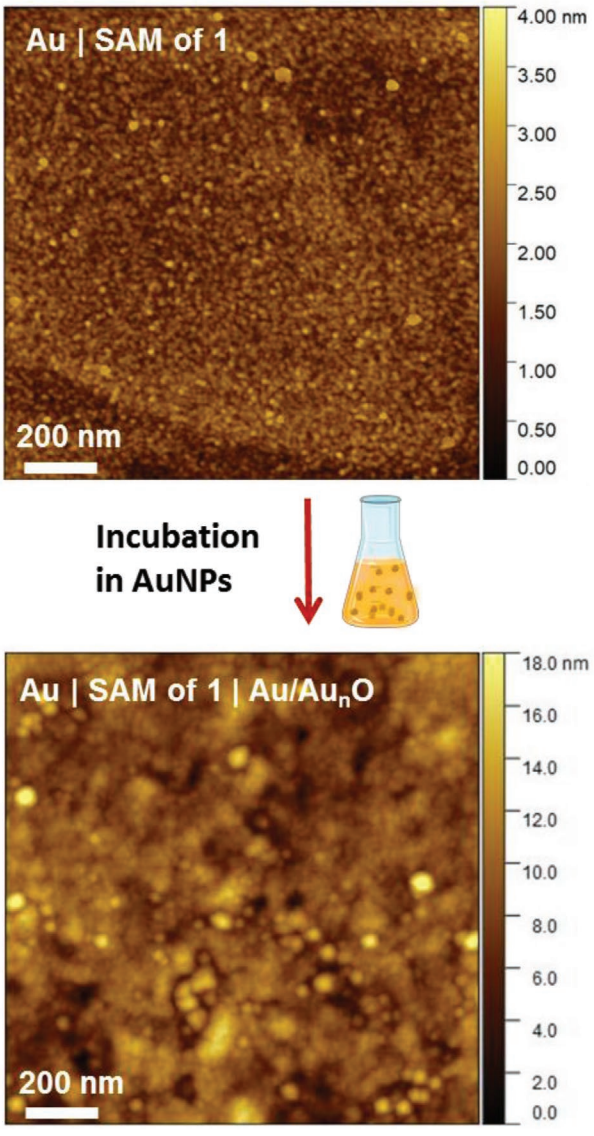

Figure 2. AFM images of pristine Au | SAM of **1** system (top panel) and Au | SAM of **1** | (Au/Au_nO)NP system (bottom panel). Gold-on-mica substrates were used in both cases.

© 2021 The Authors. Advanced Materials Interfaces published by Wiley-VCH GmbH

of **1** completely blocks the gold electrode, which is indicative of a very compact monolayer with a remarkably low occurrence of pores or holes (Figure S5, Supporting Information).[87] AFM images of SAMs of **1** further confirmed the formation of a homogenous and tightly-packed organic layer (**Figure 2**, top panel). By scratching the film with the AFM tip,[87] the average thickness of the monolayer film of **1** was determined to be (1.78 ± 0.14 nm) nm.[58] Consistent with this result, XPS experiments determined a film thickness of (1.85 ± 0.05) nm.[58] The topographic study of the SAM of **1** by AFM indicated a root mean square (RMS) roughness of (0.5 ± 0.1) nm.[58]

A gold-on-mica supported Au | SAM of **1** was immersed in an aqueous dispersion of the (Au/Au_nO)NPs with concentration 2.265 mg Au · L^{-1}, as determined from inductively coupled plasma atomic emission spectroscopy, and the nanoparticles allowed to self-assemble on the reactive amine moieties exposed on the top surface of the monolayer. After self-assembly, AFM images of the resulting surface show a quite different topography from the pristine Au | SAM of **1** system (Figure 2), with a significantly higher RMS roughness of (2.3 ± 0.4) nm.

Analysis of surface images from both AFM and SEM techniques indicate that rather than a scattering of discrete (Au/Au_nO)NPs over the monolayer, the surface features a more complete coverage of the monolayer by a condensed film which is free of pin holes and relatively uniform in height, albeit with some 3D protrusions that roughen the surface (Figure S6, Supporting Information). Depth profiling of the nascent Au | SAM of **1** | (Au/Au_nO)NP junction was undertaken by scratching of the surface with the AFM tip to determine the thickness of the sandwich structure (12.6 ± 0.5 nm; Figure S7, Supporting Information). Taking into account the thickness of the SAM of **1** (≈1.8 nm) the top gold layer has an estimated total thickness of ≈10.8 nm. A further threshold depth statistical analysis on three different regions of the same Au | SAM of **1** | (Au/Au_nO) NP system were analyzed by AFM (**Figure 3**). Holes with the threshold depth indicated in the top arrow, are shown by the blue colored regions in each panel of Figure 3. Below each AFM image, the corresponding hole coverage is reported with respect to the whole AFM image: remarkably, for each region, no holes can be detected if a threshold depth of −9 nm or lower is selected. This observation is indicative of an excellent coverage of the underlying organic film by the gold film layer, close to 100%.

The initial self-assembly of the uncapped gold nanoparticles onto the amine-terminated monolayer seems chemically sensible, while the spontaneous sintering process at room temperature may be triggered by the remarkable enthalpy of reaction which arises from the reduction of the surface area of the gold nanoparticles.[88] The deposited film was also analyzed by XPS (**Figure 4**); in order to avoid ambiguity from a gold signal arising from the bottom substrate, for this particular experiment a silver-on-glass substrate was used. A SAM of **1** was deposited onto an Ag-on-glass substrate and subsequently the monolayer was incubated in a (Au/Au_nO)NPs aqueous dispersion with the subsequent formation of a gold film. The XPS spectrum collected from the resulting structure clearly shows the presence of Au(0), with two peaks at 84.1 and 87.7 eV attributed to the $4f_{7/2}$ and $4f_{5/2}$ signals of gold. Additional $4f_{7/2}$ and $4f_{5/2}$ signals at 84.6 and 88.2 eV indicate the presence of lower gold oxides, Au_2O or AuO. The amount of gold oxide is estimated to be ≈9% from the XPS peak integration, which is in good agreement with the estimated value of the pristine AuNPs as prepared by the thermolysis of AuNC@LP at 500 °C (≈9%, Figure S3, Supporting Information). Given that Au_2O has been reported before to be a direct narrowband-gap semiconductor[89] the ≈91% of Au(0) and ≈9% gold oxides film on top of the large area junctions is expected to exhibit a nearly metallic character, with conducting properties that will allow its use as a top-contact electrode in molecular electronics. Additionally, the XPS survey spectrum (Figure S8, Supporting Information) gives no evidence of extraneous material, which strongly supports the notion that the (Au/Au_nO)NPs prepared in this manner are truly uncapped and do not feature significant adsorption of any other material from air.

The electrochemical activity of the $K_3[Fe(CN)_6]$ redox probe is completely inhibited when a gold substrate modified by a SAM of **1** is used as the working electrode (Figure S5, Supporting Information).[58] This result is indicative of the formation of a tightly-packed monolayer free of holes.[85] Importantly, the deposition of the top contact Au/Au_nO film onto such a SAM of **1** modified gold electrode results in a partial recovery of the activity of the underlying electrode, allowing detection of the Faradaic current due to the $K_3[Fe(CN)_6]$ redox probe in solution (Figure S5, Supporting Information). Many contributions in the literature have shown that after deposition of conducting nanostructures onto modified electrodes incorporating insulating organic layers that completely block the electron transfer (ET), the Faradaic electrochemistry can be partially or completely restored. In fact, this phenomenon has been reported for systems where disruption of the SAM by penetration of the conducting nanostructures trough the layer was ruled out by experimental evidence.[90] Examples include metallic,[91] organometallic,[92] quantum dot,[93] or carbon-based materials[94,95] deposited onto organic monolayers. This has been attributed to a "relay station" effect of these conducting nanostructures that promotes the electronic coupling between the underlying electrode and the redox probe.[96] The ET mechanism in these electrode | monolayer | conducting nanostructure systems is therefore the result of two consecutive steps: i) ET between the electrode and the conducting nanostructures, mediated by electron tunneling through the organic film, and ii) ET between the conducting nanostructures and the redox probe. In order to confirm that this partial restoration of the electrode activity is due to the above described relay station effect and not due to defects generated upon the adsorption of the (Au/Au_nO)NPs, c-AFM studies have been carried out to assess the presence or absence of pinholes and short circuits. Thus, the electrical characteristics of the Au | SAM of **1** | Au/Au_nO system were determined from the current–voltage (*I*–*V*) curves collected with a conducting-AFM (Bruker ICON) operating in the peak force tunneling AFM (PF-TUNA) mode by locating the AFM tip on top of the gold film. This mode was used to limit physical damage to the surface by the tip during measurement; in this method an intermittent contact (at a frequency of 2 kHz) between the AFM tip and the sample surface takes place with a low maximum normal force (peak-force) and limited lateral forces.[56,58–60,97,98]

Before recording the *I*–*V* curves, the most suitable contact force to be applied to the Au | SAM of **1** | Au/Au_nO junctions

© 2021 The Authors. Advanced Materials Interfaces published by Wiley-VCH GmbH

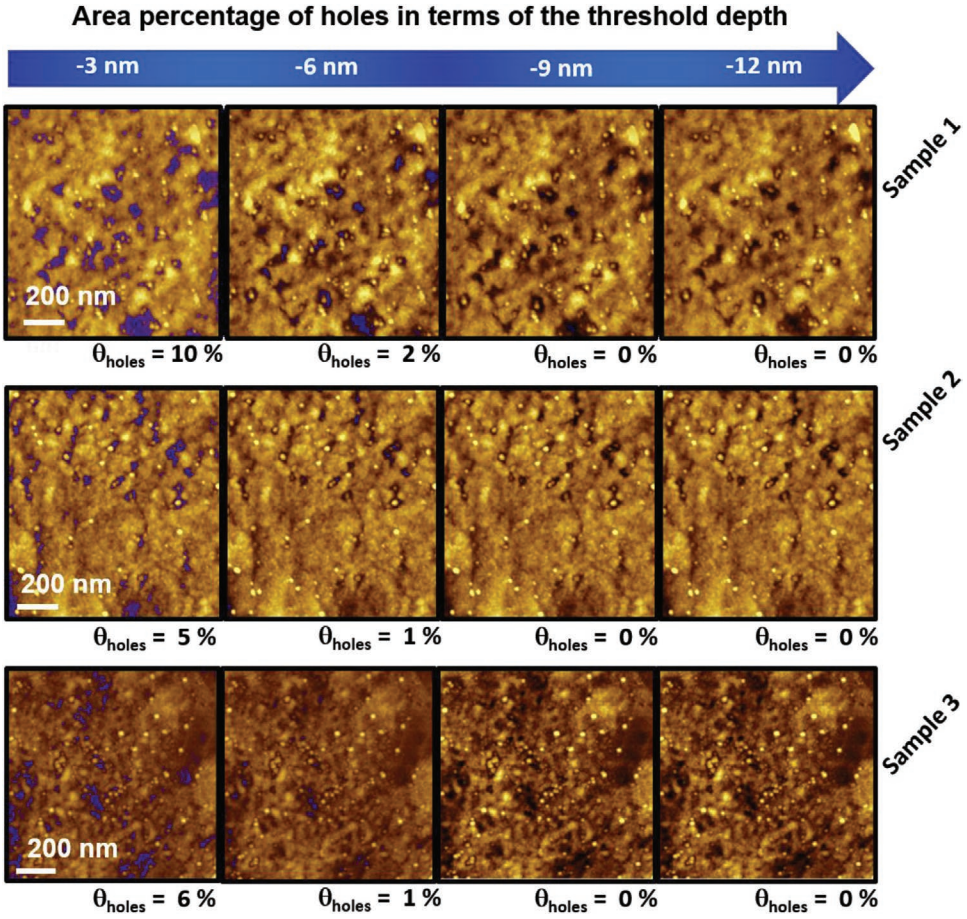

Figure 3. AFM images of three different Au | SAM of **1** | (Au/Au$_n$O)NP regions. For each of them, a threshold depth statistical analysis is shown, highlighting in blue color, the morphological holes showing the specified depth in the top blue arrow. Below each AFM image, the corresponding hole coverage is reported.

was determined to ensure an appropriate balance between a poor electrical contact between the AFM probe and the gold film (contact force too low) and an unacceptably large deformation of the SAM of **1** (contact force too high). In making this

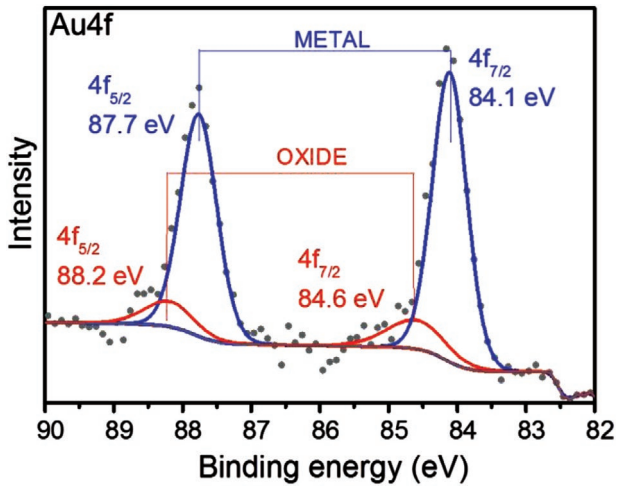

Figure 4. XPS spectrum of an Ag | SAM of **1** | Au/Au$_n$O structure.

estimation, the ≈8% uncertainty in the set-point force due to the calibration method (thermal tuning) used to estimate the nominal spring constant needs to be taken into account.[99] The average conductance values (obtained from the slope of the linear fit of the average *I*–*V* curve in the ohmic region (from –0.4 to 0.4 V)) as a function of the set-point force are shown in **Figure 5**a. At set-point forces between 8.5 and 17 nN the current through the junction was practically negligible, indicating poor electrical contact between the tip and the gold film. A set-point force of 35 nN was the minimum value that resulted in a significant conductance through the junction indicating a good electrical contact between the tip and the Au/Au$_n$O top-contact electrode, indicating the onset of contact between the tip and the film. A further increase in the set-point force (40.3 or 45.6 nN) results in higher junction conductance values as the tip protrudes into the junction. For these reasons, *I*–*V* curves were recorded by locating the AFM tip on top of the gold film at 35 and 40.3 nN set-point forces (Figure 5b). Additionally, *I*–*V* curves were also recorded for a set-point force of 45.6 nN (Figure S9, Supporting Information). The tip voltage was swept (±1.0 V) with the bottom gold substrate held at ground. To ensure the reproducibility and the reliability of the results, *I*–*V* curves at each set-point force were obtained by placing the

© 2021 The Authors. Advanced Materials Interfaces published by Wiley-VCH GmbH

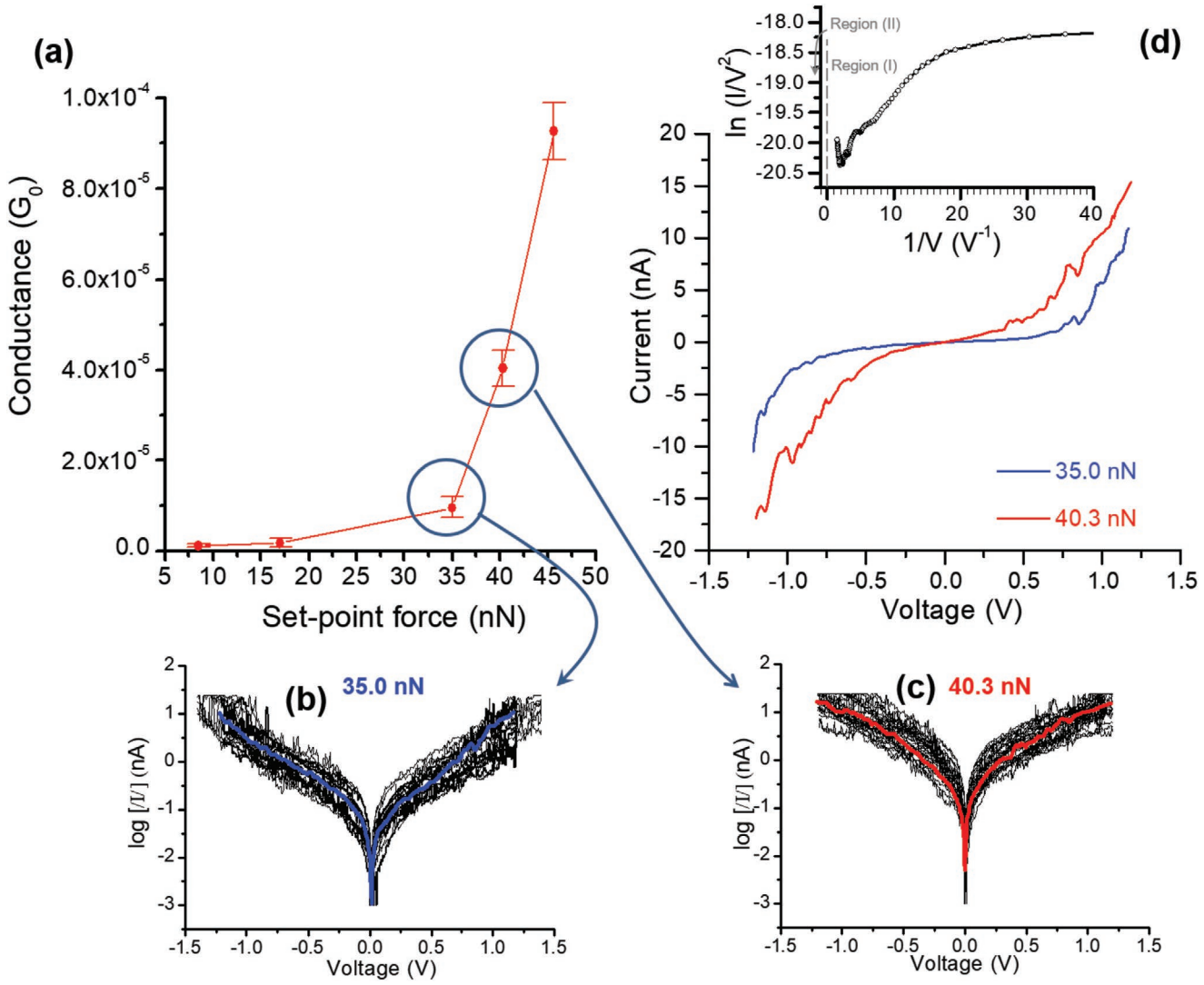

Figure 5. a) Conductance values determined by locating the tip of the c-AFM onto the top electrode versus the applied set point-force. Log[|*I*|] versus voltage measured at a set point force of b) 35 and c) 40.3 nN. In blue and red line, the average curves. d) Average *I*–*V* curve for an Au | SAM of **1** | Au/Au$_n$O junction at the indicated set-point forces obtained by positioning the c-AFM tip on top of the Au layer. Inset figure: Fowler–Nordheim plot for a set-point force of 35 nN.

conductive AFM tip on the Au/Au$_n$O top-contact electrode at different locations in the sample as well as using three different samples. Figure 5b,c shows the *I*–*V* curves recorded as well as the average one (blue and red line) at the set-point forces (35 and 40.3 nN), that ensure good electrical contact between the tip and the Au/Au$_n$O top-contact electrode (Figure 5a). A variation of less than half an order of magnitude in the obtained current demonstrates the reproducibility, reliability, and low fluctuations of the Au | SAM of **1** | Au/Au$_n$O system. Importantly, all the *I*–*V* curves feature the characteristic sigmoidal shape recorded for metal–molecule–metal junctions rather than of linear ohmic traces indicative of metallic short circuits, indicating that the deposition of the top contact neither damages the underlying SAM, nor alters or contaminates the interfaces.

The transition voltage (V_{trans}) was determined from the inflection point in the Fowler–Nordheim plot when a set-point force of 35 nN (Figure 5b) or 40.3 nN (Figure S10, Supporting Information) were used. In both cases, the logarithm of the current scales with 1/*V* in the low-bias regime (region I in the inset of Figure 5b), which points to direct tunneling. In region II, a negative slope with the current scaling linearly with 1/*V* is obtained, corresponding to field emission. From the inset of Figure 5b, a very low V_{trans} value of 0.49 V is obtained. Since the measurement of V_{trans} provides a means of experimentally estimating the height of the original rectangular barrier, the low obtained value for V_{trans} suggests a good alignment between the metal Fermi level and the frontier molecular orbitals in these molecular junctions since, as indicated, V_{trans} is linearly correlated with, though not directly equal to, the energy difference between the frontier molecular orbital level and the metal Fermi level.[99,100] The good alignment between the metal Fermi level and the frontier molecular orbital levels is corroborated by the very similar value for V_{trans}, 0.52 V, obtained at a set-point force of 40.3 nN (Figure S10, Supporting Information).

© 2021 The Authors. Advanced Materials Interfaces published by Wiley-VCH GmbH

3. Conclusions

In this contribution nascent Au | SAM of **1** | Au/Au$_n$O large area junctions have been prepared. These junctions were fabricated by soft, simple, and low-cost self-assembly methodologies which are highly reproducible and easily scalable. First the organic monolayer was deposited by self-assembly onto a gold bottom-electrode. Second, this Au| SAM of **1** system was incubated in a dispersion of uncapped gold nanoparticles. These nanoparticles were prepared by thermolysis of lipoic capped AuNC, with these gold nanoparticles being stabilized by the presence of a certain amount of gold oxide (≈9%) and negatively adsorbed ions. The resulting junctions exhibit a large (≈100%) surface coverage of the organic monolayer by a thin film of Au/Au$_n$O prepared from coalesced uncapped gold nanoparticles. A high yield (no short-circuits have been detected) and a good electrical performance with a very low transition voltage has been proven. Taken together this contribution opens the door to the use of metal uncapped gold nanoparticles stabilized by gold oxide in a low proportion for the fabrication of the top contact electrode. Additionally, if required, an improvement of the electrical conductivity of the gold film might be achieved by the application of subsequent chemical or electrochemical steps by reducing the small fraction of gold oxide film after its deposition on the film. This methodology may also be used for metallization of thin organic films for other applications such as modified electrodes, (bio)sensors, etc. Further studies in these directions are underway.

4. Experimental Section

Fabrication of the Au | SAM of **1**: Compound **1** (Figure 1) was prepared as previously described.[101] Gold substrates (Arrandee, Schroeder, Germany) were flame-annealed at ≈800–1000 °C with a Bunsen burner flame immediately prior to use in a manner known to give atomically flat Au(111) terraces.[102] Gold-on-mica (Georg Albert PVD Beschichtunben, Germany) and silver-on-glass (Arrandee, Germany) substrates were purchased and used as received. SAMs of **1** were prepared by immersion of the substrate (annealed gold-on-glass, gold-on-mica, or silver-on-glass) in a 10^{-4} M solution of **1** in tetrahydrofuran (THF, HPLC grade ≥99.9%, inhibitor-free solution) for 48 h at room temperature. After incubation of the substrate in the solution, the monolayers of **1** were thoroughly rinsed with THF to remove any physisorbed material and dried under a stream of dry nitrogen. The surface coverage of the monolayer of **1** was determined using a QCM from Stanford Research Systems instrument. AT-cut, α-quartz crystals with a resonant frequency of 5 MHz and circular gold electrodes patterned on both sides were used.

Synthesis and Characterization of the Gold Nanoparticles: Uncapped gold nanoparticles were prepared by thermolysis of lipoic acid stabilized AuNC (AuNCs@LP), which were synthesized according to the procedure described by Aldeek et al.[80] To prepare the gold nanoparticles, the AuNCs@LP stock solution (150 mL, 2.265 mg Au L^{-1} in water) was placed in a Pyrex vessel and heated to a temperature of 500 °C in a muffle furnace for 1 h. After this time, the vessel was allowed to cool to room temperature and residue taken up in Milli-pore Milli-Q water (50 mL), the mixture sonicated for 15 min and the suspension allowed to settle for 2 h before the solution was separated from the insoluble ash by decantation. The resulting aqueous gold nanoparticle dispersions were characterized by UV–vis absorption spectroscopy in a quartz cell (HP8453 Agilent UV–vis spectrophotometer). In addition, the 3D fluorescence spectrum of these (Au/Au$_n$O)NPs was recorded with a Cary Eclipse fluorescence spectrometer (10 nm excitation and fluorescence slits, λ_{exc} = 200–600 nm and λ_{em} = 250–850 nm). Whilst this procedure gave gold nanoparticles with reliable reproducibility in the dispersion of sizes and optical properties of the nanoparticles, the optical characterization of the gold nanoparticles obtained at other pyrolysis temperatures is also shown in the Section S1, Supporting Information for completeness. The AuNCs@LP clusters and the gold nanoparticles were analyzed by XPS, where the supporting substrate was silicon oxide. XPS was performed in a Kratos AXIS ultraDLD spectrophotometer including a monochromatic Al Kα X-ray source (1486.6 eV) and a pass energy of 20 eV. XPS binding energies were referenced to the C1s peak at 284.6 eV.

A Tecnai F30 microscope capable of operating in both scanning and transmission mode (STEM; FEI, The Netherlands) was used to characterize the shape and size of the AuNPs. The hydrodynamic diameter of these (Au/Au$_n$O)NPs and polydispersity were determined using a particle size analyzer (Plus Particle Size-Analyser, Brookhaven Instruments Corporation) based on the time dependent fluctuation of DLS of a laser by the nanoparticles (Section S1, Supporting Information). This equipment was also used to determine the electrophoretic mobility (ζ potential) of the (Au/Au$_n$O)NPs by measuring the surface potential of a 0.01 mg·mL^{-1} suspension of the (Au/Au$_n$O)NPs sample in 1 mM KCl at 25 °C with a zeta potential analyzer using Zeta Plus software. The measurement of zeta potential was based on the direction and velocity of particles under the influence of a known electric field.

Characterization of the Au | SAM of **1** *| Au/Au$_n$O Junctions*: AFM images were obtained in tapping mode using a Multimode 8 AFM microscope equipped with a Nanoscope V control unit from Bruker operating in ambient air conditions at a scan rate of 0.5–1.2 Hz. RTESPA-150 cantilevers (resonance frequency ≈ 150 kHz, force constant ≈ 6 N·m^{-1}, nominal values, ≈10 nm radius), purchased from Bruker, were used. All the scratches were achieved in contact mode (scan rate 3 Hz), selecting a high deflection set point (about 2 V) in order to apply a strong force (higher than 100 nN) onto the sample and remove the organic material.[87] The RMS roughness, surface coverage, and height/depth statistical analysis were carried out using the Gwyddion v. 2.41 package software. A conductive-AFM (Bruker ICON) under humidity control (≈40% by dry N_2 flux) using the PF-TUNA mode was employed to determine the electrical properties of the Au | SAM of **1** | Au/Au$_n$O junctions. This study was carried out using a PF-TUNA cantilever from Bruker (coated with Pt/Ir 20 nm, ≈25 nm radius, 0.4 N m^{-1} spring constant and 70 kHz resonance frequency), which was previously calibrated by the thermal tuning method.[103]

CV experiments were performed using a potentiostat from EcoChemie and a standard three electrode cell, where the working electrode was a bare Au (111) electrode, an Au(111) electrode covered by a monolayer of **1**, or Au(111) electrode covered by a monolayer of **1** after incubation in (Au/Au$_n$O)NPs. These working electrodes were connected to the potentiostat by means of a cable ended in a metallic tweezer that held the electrode. The reference electrode was Ag/AgCl, KCl (3 M) and the counter electrode was a Pt sheet.

Supporting Information

Supporting Information is available from the Wiley Online Library or from the author.

Acknowledgements

P.C., J.L.S., S. Martín, and J.G. are grateful for financial assistance from Ministerio de Ciencia e Innovación from Spain and fondos FEDER in the framework of projects PID2019-105881RB-I00, PID2019-105408GB-I00, and PGC2018-097583-B-I00. J.L.S. also acknowledges the funded project Hierarchical Self Assembly of Polymeric Soft Systems, "SASSYPOL," from the 7th Framework Programme (CEE, Ref-607602). L.H., S. Martín, J.L.S, P.C., S. de Marcos, and J.G. acknowledge support from DGA/Fondos FEDER (construyendo Europa desde Aragón) for funding

© 2021 The Authors. Advanced Materials Interfaces published by Wiley-VCH GmbH

PLATON (E31_20R), CLIP (E47_17R) and N&SB (E25_17R) research groups. P.J.L. gratefully acknowledges support from the Australian Research Council (DP190100073; DP190100074). R.S. is grateful for the support provided by PASPA of the DGAPA and Engineering Faculty of National Autonomous University of Mexico.

Conflict of Interest

The authors declare no conflict of interest.

Author Contributions

A.M.-B., R.S., S.C., and A.G.-S. contributed equally to this work. A.M.-B., S. de Marcos, and J.G. carried out the synthesis and characterization of the nanoparticles. R.S., A.G.-S., and L.H. worked on the deposition of the monolayer and the top-contact electrode. S.C. and Santiago Martín performed and analyzed the AFM and XPS experiments, respectively. L.H., J.L. S., and P.J.L. designed and synthesized the sample of **1** used in this study. F.P.-M., S. Martín, and P.C. carried out the experimental studies of the electrical properties, and provided the interpretation of these results. P.J.L., J.G., and P.C. wrote the paper with the contribution of the rest of the authors. J.G. and P.C. conceived the hypothesis of this work, supervised the project, and coordinated the experiments.

Data Availability Statement

Research data are not shared.

Keywords

molecular electronics, self-assembly methods, stable uncapped gold nanoparticles, top-contact electrode

Received: May 31, 2021
Revised: July 12, 2021
Published online:

[1] D. Xiang, X. L. Wang, C. C. Jia, T. Lee, X. F. Guo, *Chem. Rev.* **2016**, *116*, 4318.
[2] S. Marques-Gonzalez, P. J. Low, *Aust. J. Chem.* **2016**, *69*, 244.
[3] Y. Komoto, S. Fujii, M. Iwane, M. Kiguchi, *J. Mater. Chem. C* **2016**, *4*, 8842.
[4] R. J. Nichols, W. Haiss, S. J. Higgins, E. Leary, S. Martin, D. Bethell, *Phys. Chem. Chem. Phys.* **2010**, *12*, 2801.
[5] R. L. McCreery, A. J. Bergren, *Adv. Mater.* **2009**, *21*, 4303.
[6] L. Wang, L. Wang, L. Zhang, D. Xiang, *Top. Curr. Chem.* **2017**, *375*, 61.
[7] L. A. Bumm, J. J. Arnold, M. T. Cygan, T. D. Dunbar, T. P. Burgin, L. Jones, II, D. L. Allara, J. M. Tour, P. S. Weiss, *Science* **1996**, *271*, 1705.
[8] C. Jia, A. Migliore, N. Xin, S. Huang, D. Wang, B. Feng, Z. Liu, G. Zhang, D.-H. Qu, H. Tian, M. A. Ratner, H. Q. Xu, A. Nitzan, X. Guo, *Science* **2016**, *352*, 1443.
[9] B. Capozzi, J. Xia, O. Adak, E. J. Dell, Z.-F. Liu, J. C. Taylor, J. B. Neaton, L. M. Campos, L. Venkataraman, *Nat. Nanotechnol.* **2015**, *10*, 522.
[10] G. Jayamurugan, V. Gowri, D. Hernández, S. Martín, A. González-Orive, C. Dengiz, O. Dumele, F. Pérez-Murano, J.-P. Gisselbrecht, C. Boudon, W. B. Schweizer, B. Breiten, A. D. Finke, G. Jeschke, B. Bernet, L. Ruhlmmann, P. Cea, F. Diederich, *Chem. - Eur. J.* **2016**, *22*, 10539.
[11] H. M. Osorio, S. Catarelli, P. Cea, J. B. G. Gluyas, F. Hartl, S. J. Higgins, E. Leary, P. J. Low, S. Martin, R. J. Nichols, J. Tory, J. Ulstrup, A. Vezzoli, D. C. Milan, Q. Zeng, *J. Am. Chem. Soc.* **2015**, *137*, 14319.
[12] M. H. Garner, H. Li, Y. Chen, T. A. Su, Z. Shangguan, D. W. Paley, T. Liu, F. Ng, H. Li, S. Xiao, C. Nuckolls, L. Venkataraman, G. C. Solomon, *Nature* **2018**, *558*, 415.
[13] *Nat. Nanotechnol.* **2013**, *8*, 377.
[14] K. Wang, E. Meyhofer, P. Reddy, *Adv. Funct. Mater.* **2020**, *30*, 1904534.
[15] S. Park, H. Kang, H. J. Yoon, *J. Mater. Chem. A* **2019**, *7*, 14419.
[16] S. K. Saxena, U. M. Tefashe, M. Supur, R. L. McCreery, *ACS Sens.* **2021**, *6*, 513.
[17] I. J. Planje, R. J. Davidson, A. Vezzoli, A. Daaoub, S. Sangtarash, H. Sadeghi, S. Martín, P. Cea, C. J. Lambert, A. Beeby, S. J. Higgins, R. J. Nichols, *ACS Sens.* **2021**, *6*, 530.
[18] G. Reecht, F. Scheurer, V. Speisser, Y. J. Dappe, F. Mathevet, G. Schull, *Phys. Rev. Lett.* **2014**, *112*, 047403.
[19] Y. Li, N. L. Haworth, L. Xiang, S. Ciampi, M. L. Coote, N. Tao, *J. Am. Chem. Soc.* **2017**, *139*, 14699.
[20] M. C. Walkey, C. R. Peiris, S. Ciampi, A. C. Aragonès, R. B. Domínguez-Espíndola, D. Jago, T. Pulbrook, B. W. Skelton, A. N. Sobolev, I. Díez Pérez, M. J. Piggott, G. A. Koutsantonis, N. Darwish, *ACS Appl. Mater. Interfaces* **2019**, *11*, 36886.
[21] A. C. Aragonès, N. L. Haworth, N. Darwish, S. Ciampi, N. J. Bloomfield, G. G. Wallace, I. Diez-Perez, M. L. Coote, *Nature* **2016**, *531*, 88.
[22] S. Ciampi, N. Darwish, H. M. Aitken, I. Díez-Pérez, M. L. Coote, *Chem. Soc. Rev.* **2018**, *47*, 5146.
[23] T. A. Su, M. Neupane, M. L. Steigerwald, L. Venkataraman, C. Nuckolls, *Nat. Rev. Mater.* **2016**, *1*, 16002.
[24] F. Pauly, J. K. Viljas, U. Huniar, M. Häfner, S. Wohlthat, M. Bürkle, J. C. Cuevas, G. Schön, *New J. Phys.* **2008**, *10*, 125019.
[25] D. Xiang, X. Wang, C. Jia, T. Lee, X. Guo, *Chem. Rev.* **2016**, *116*, 4318.
[26] A. R. Rocha, V. M. Garcia-Suarez, S. Bailey, C. Lambert, J. Ferrer, S. Sanvito, *Phys. Rev. B: Condens. Matter Mater. Phys.* **2006**, *73*, 085414.
[27] J. E. Green, J. W. Choi, A. Boukai, Y. Bunimovich, E. Johnston-Halperin, E. DeIonno, Y. Luo, B. A. Sheriff, K. Xu, Y. S. Shin, H. R. Tseng, J. F. Stoddart, J. R. Heath, *Nature* **2007**, *7126*, 414.
[28] A. J. Bergren, L. Zeer-Wanklyn, M. Semple, N. Pekas, B. Szeto, R. L. McCreery, *J. Phys.: Condens. Matter* **2016**, *9*, 094011.
[29] J. G. Kushmerick, D. B. Holt, S. K. Pollack, M. A. Ratner, J. C. Yang, T. L. Schull, J. Naciri, M. H. Moore, R. Shashidhar, *J. Am. Chem. Soc.* **2002**, *124*, 10654.
[30] D. Vuillaume, *C. R. Phys.* **2008**, *9*, 78.
[31] H. Haick, D. Cahen, *Prog. Surf. Sci.* **2008**, *83*, 217.
[32] H. B. Akkerman, B. de Boer, *J. Phys.: Condens. Matter* **2008**, *20*, 013001.
[33] D. Vuillaume, *Proc. IEEE* **2010**, *98*, 2111.
[34] A. V. Walker, *J. Vac. Sci. Technol., A* **2013**, *31*, 050816.
[35] L. Herrer, S. Martín, P. Cea, *Appl. Sci.* **2020**, *10*, 6064.
[36] E. Gorenskaia, K. L. Turner, S. Martín, P. Cea, P. J. Low, *Nanoscale* **2021**, *13*, 9055.
[37] E. Leary, M. T. González, C. van der Pol, M. R. Bryce, S. Filipone, N. Martin, G. Rubio-Bollinger, N. Agrait, *Nano Lett.* **2011**, *11*, 2236.
[38] L. Costelle, M. T. Räisänen, J. T. Joyce, C. Silien, L.-S. Johansson, J. M. Campbell, J. Räisänen, *J. Phys. Chem. C* **2012**, *116*, 22602.
[39] R. Lovrinčić, O. Kraynis, R. Har-Lavan, A.-E. Haj-Yahya, W. Li, A. Vilan, D. Cahen, *J. Phys. Chem. Lett.* **2013**, *4*, 426.
[40] R. M. Metzger, T. Xu, I. R. Peterson, *J. Phys. Chem. B* **2001**, *105*, 7280.
[41] R. T. W. Popoff, K. K. Kavanagh, H.-Z. Yu, *Nanoscale* **2011**, *3*, 1434.
[42] A. Scott, D. B. Janes, C. Risko, M. A. Ratner, *Appl. Phys. Lett.* **2007**, *91*, 033508.

© 2021 The Authors. Advanced Materials Interfaces published by Wiley-VCH GmbH

[43] Z. Shi, P. Lu, A. V. Walker, *Langmuir* **2012**, *28*, 16909.
[44] A. V. Walker, T. B. Tighe, O. M. Cabarcos, M. D. Reinard, B. C. Haynie, S. Uppili, N. Winograd, D. L. Allara, *J. Am. Chem. Soc.* **2004**, *126*, 3954.
[45] Z. Zhu, D. L. Allara, N. Winograd, *Appl. Surf. Sci.* **2006**, *252*, 6686.
[46] R. Har-Lavan, O. Yaffe, P. Joshi, R. Hazaz, H. Cohen, D. Cahen, *AIP Adv.* **2012**, *2*, 012164.
[47] O. Yaffe, L. Scheres, L. Segev, A. Biller, I. Ron, E. Salomon, M. Giesbers, A. Kahn, L. Kronik, H. Zuilhof, A. Vilan, D. Cahen, *J. Phys. Chem. C* **2010**, *114*, 10270.
[48] H. Yan, A. J. Bergren, R. L. McCreery, *J. Am. Chem. Soc.* **2011**, *133*, 19168.
[49] S. Sangiao, S. Martin, A. Gonzalez-Orive, C. Magen, P. J. Low, J. M. de Teresa, P. Cea, *Small* **2017**, *13*, 1603207.
[50] S. Pookpanratana, J. W. F. Robertson, C. Jaye, D. A. Fischer, C. A. Richter, C. A. Hacker, *Langmuir* **2013**, *29*, 2083.
[51] Y. L. Loo, D. V. Lang, J. A. Rogers, J. W. P. Hsu, *Nano Lett.* **2003**, *3*, 913.
[52] Y. D. Chiu, W. P. Dow, K. Krug, Y. F. Liu, Y. L. Lee, S. L. Yau, *Langmuir* **2012**, *28*, 14476.
[53] C. Silien, D. Lahaye, M. Caffio, R. Schaub, N. R. Champness, M. Buck, *Langmuir* **2011**, *27*, 2567.
[54] A. P. Bonifas, R. L. McCreery, *Nat. Nanotechnol.* **2010**, *5*, 612.
[55] S. Martin, G. Pera, L. M. Ballesteros, A. J. Hope, S. Marqués-González, P. J. Low, F. Perez-Murano, R. J. Nichols, P. Cea, *Chem. - Eur. J.* **2014**, *20*, 3421.
[56] S. Martín, L. M. Ballesteros, A. González-Orive, H. Oliva, S. Marqués-González, M. Lorenzoni, R. Nichols, F. Pérez-Murano, P. J. Low, P. Cea, *J. Mater. Chem. C* **2016**, *4*, 9036.
[57] H. M. Osorio, P. Cea, L. M. Ballesteros, I. Gascon, S. Marqués-González, R. J. Nichols, F. Pérez-Murano, P. J. Low, S. Martín, *J. Mater. Chem. C* **2014**, *2*, 7348.
[58] L. Herrer, V. Sebastian, S. Martin, A. Gonzalez-Orive, F. Perez-Murano, P. J. Low, J. L. Serrano, J. Santamaria, P. Cea, *Nanoscale* **2017**, *9*, 13281.
[59] L. M. Ballesteros, S. Martin, J. Cortés, S. Marqués-Gonzalez, F. Pérez-Murano, R. J. Nichols, P. J. Low, P. Cea, *Adv. Mater. Interfaces* **2014**, *1*, 1400128.
[60] R. Ezquerra, S. G. Eaves, S. Bock, B. W. Skelton, F. Pérez-Murano, P. Cea, S. Martin, P. J. Low, *J. Mater. Chem. C* **2019**, *19*, 6630.
[61] G. Puebla-Hellmann, K. Venkatesan, M. Mayor, E. Lörtscher, *Nature* **2018**, *559*, 232.
[62] Y.-C. Yeh, B. Creran, V. M. Rotello, *Nanoscale* **2012**, *4*, 1871.
[63] J. H. Li, R. Li, C. H. Chiang, Y. S. Zhong, H. X. Shen, E. M. Song, M. Hill, S. M. Won, K. J. Yu, J. M. Baek, Y. Lee, J. Viventi, Y. G. Huang, J. A. Rogers, *Adv. Mater. Technol.* **2020**, *5*, 1900800.
[64] S. Choi, S. I. Han, D. Jung, H. J. Hwang, C. Lim, S. Bae, O. K. Park, C. M. Tschabrunn, M. Lee, S. Y. Bae, J. W. Yu, J. H. Ryu, S. W. Lee, K. Park, P. M. Kang, W. B. Lee, R. Nezafat, T. Hyeon, D. H. Kim, *Nat. Nanotechnol.* **2018**, *13*, 1048.
[65] K. Saha, S. S. Agasti, C. Kim, X. Li, V. M. Rotello, *Chem. Rev.* **2012**, *112*, 2739.
[66] J. Zheng, C. Zhou, M. Yu, J. Liu, *Nanoscale* **2012**, *4*, 4073.
[67] W. Haiss, N. T. K. Thanh, J. Aveyard, D. G. Fernig, *Anal. Chem.* **2007**, *79*, 4215.
[68] H. Wei, S. M. H. Abtahi, P. J. Vikesland, *Environ. Sci.: Nano* **2015**, *2*, 120.
[69] Z. Yuan, C.-C. Hu, H.-T. Chang, C. Lu, *Analyst* **2016**, *141*, 1611.
[70] H. Aldewachi, T. Chalati, M. N. Woodroofe, N. Bricklebank, B. Sharrack, P. Gardiner, *Nanoscale* **2018**, *10*, 18.
[71] J. Van Rie, W. Thielemans, *Nanoscale* **2017**, *9*, 8525.
[72] M. Lafuente, S. Ruiz-Rincon, R. Mallada, P. Cea, M. P. Pina, *Appl. Surf. Sci.* **2020**, *506*, 144663.
[73] A. Martín-Barreiro, S. de Marcos, J. Galbán, *Microchim. Acta* **2018**, *185*, 171.
[74] A. Martín-Barreiro, S. de Marcos, J. M. de la Fuente, V. Grazú, J. Galbán, *Sens. Actuators, B* **2018**, *277*, 261.
[75] G. Merga, N. Saucedo, L. C. Cass, J. Puthussery, D. Meisel, *J. Phys. Chem. C* **2010**, *114*, 14811.
[76] K. Ghandi, A. D. Findlater, Z. Mahimwalla, C. S. MacNeil, E. Awoonor-Williams, F. Zahariev, M. S. Gordon, *Nanoscale* **2015**, *7*, 11545.
[77] M. A. El-Sayed, *Acc. Chem. Res.* **2001**, *34*, 257.
[78] D. Zhang, B. Gökce, S. Barcikowski, *Chem. Rev.* **2017**, *117*, 3990.
[79] M. De Anda Villa, J. Gaudin, D. Amans, F. Boudjada, J. Bozek, R. Evaristo Grisenti, E. Lamour, G. Laurens, S. Macé, C. Nicolas, I. Papagiannouli, M. Patanen, C. Prigent, E. Robert, S. Steydli, M. Trassinelli, D. Vernhet, A. Lévy, *Langmuir* **2019**, *35*, 11859.
[80] F. Aldeek, M. A. H. Muhammed, G. Palui, N. Zhan, H. Mattoussi, *ACS Nano* **2013**, *7*, 2509.
[81] P. Zhang, T. K. Sham, *Phys. Rev. Lett.* **2003**, *24*, 245502.
[82] L. Ono, B. R. Cuenya, *J. Phys. Chem. C* **2008**, *112*, 4576.
[83] L. S. Kibis, A. I. Stadnichenko, S. V. Koscheev, A. I. Zaikovskii, A. I. Boronin, *J. Phys. Chem. C* **2015**, *119*, 2523.
[84] J. J. Pireaux, M. Liehr, P. A. Thiry, J. P. Delrue, R. Caudano, *Surf. Sci.* **1984**, *141*, 221.
[85] M. D. Porter, T. B. Bright, D. L. Allara, *J. Am. Chem. Soc.* **1987**, *109*, 3559.
[86] P. Cea, M. C. Lopez, S. Martin, A. Villares, G. Pera, I. Giner, *J. Chem. Educ.* **2009**, *86*, 723.
[87] F. Anariba, S. H. DuVall, R. L. McCreery, *Anal. Chem.* **2003**, *75*, 3837.
[88] M. J. Coutts, M. B. Cortie, M. J. Ford, A. M. McDonagh, *J. Phys. Chem. C* **2009**, *113*, 1325.
[89] H. Shi, R. Asahi, C. Stampfl, *Phys. Rev. B* **2007**, *75*, 205125.
[90] J. Zhao, C. R. Bradbury, D. J. Fermin, *J. Phys. Chem. C* **2008**, *112*, 6832.
[91] J. Zhao, M. Wasem, C. R. Bradbury, D. J. Fermin, *J. Phys. Chem. C* **2008**, *112*, 7284.
[92] S. Lhenry, J. Jalkh, Y. R. Leroux, J. Ruiz, R. Ciganda, D. Astruc, P. Hapiot, *J. Am. Chem. Soc.* **2014**, *136*, 17950.
[93] N. Kantor-Uriel, P. Roy, S. Saris, V. Kiran, D. H. Waldeck, R. Naaman, *J. Phys. Chem. C* **2015**, *119*, 15839.
[94] A. Chou, P. K. Eggers, M. N. Paddon-Row, J. J. Gooding, *J. Phys. Chem. C* **2009**, *113*, 3203.
[95] X. Xie, K. Zhao, X. Xu, W. Zhao, S. X. Liu, Z. Zhu, M. Li, Z. Shi, Y. Shao, *J. Phys. Chem. C* **2010**, *114*, 1423.
[96] J.-N. Chazalviel, P. Allongue, *J. Am. Chem. Soc.* **2011**, *133*, 762.
[97] B. Pittenger, N. Erina, D. Su, Application Note, Veeco Instruments Inc., **2010**.
[98] A. Moneo, A. González-Orive, S. Bock, M. Fenero, I. L. Herrer, D. C. Milan, M. Lorenzoni, R. J. Nichols, P. Cea, F. Perez-Murano, P. J. Low, S. Martin, *Nanoscale* **2018**, *10*, 14128.
[99] C. T. Gibson, D. A. Smith, C. J. Roberts, *Nanotechnology* **2005**, *16*, 234.
[100] J. M. Beebe, B. Kim, J. W. Gadzuk, C. D. Frisbie, J. G. Kushmerick, *Phys. Rev. Lett.* **2006**, *97*, 026801.
[101] Q. Lu, K. Liu, H. Zhang, Z. Du, X. Wang, F. Wang, *ACS Nano* **2009**, *3*, 3861.
[102] W. Haiss, D. Lackey, J. K. Sass, *J. Chem. Phys.* **1991**, *95*, 2193.
[103] J. P. Cleveland, S. Manne, D. Bocek, P. K. Hansma, *Rev. Sci. Instrum.* **1993**, *64*, 403.

© 2021 The Authors. Advanced Materials Interfaces published by Wiley-VCH GmbH